Journal of Colloid and Interface Science 429 (2014) 53–61

Contents lists available at ScienceDirect

Journal of Colloid and Interface Science

www.elsevier.com/locate/jcis

Vapor-phase hydrothermal synthesis of rutile TiO_2 nanostructured film with exposed pyramid-shaped (1 1 1) surface and superiorly photoelectrocatalytic performance

Jiangyao Chen [a,b], Haimin Zhang [b], Porun Liu [b], Yun Wang [b], Xiaolu Liu [b], Guiying Li [a], Taicheng An [a,*], Huijun Zhao [b,*]

[a] State Key Laboratory of Organic Geochemistry, Guangzhou Institute of Geochemistry, Chinese Academy of Sciences, Guangzhou 510640, China
[b] Centre for Clean Environment and Energy, Griffith University, Gold Coast Campus, QLD 4222, Australia

ARTICLE INFO

Article history:
Received 25 March 2014
Accepted 4 May 2014
Available online 22 May 2014

Keywords:
Vapor-phase hydrothermal
Rutile TiO_2 film
{1 1 1} Crystal facet
Photoelectrocatalytic
Rhodamine B

ABSTRACT

Rutile TiO_2 nanostructured film with exposed pyramid-shaped (1 1 1) surface was successfully fabricated using metal titanium foil as substrate through a facile vapor-phase hydrothermal method. The fabricated rutile TiO_2 film was composed of vertically aligned rod-like structures with diameters ranged from 400 to 700 nm and thickness of *ca.* 2.0 μm. The obtained rutile TiO_2 film as photoanode exhibited excellent photoelectrocatalytic activity toward water oxidation and rhodamine B decolorization under UV illumination, which was more than 3.5 and 1.2 times of that obtained by highly ordered anatase TiO_2 nanotube array film photoanode under the same experimental conditions, respectively. The excellent photoelectrocatalytic performance of the rutile TiO_2 film photoanode could be due to the superior photoelectron transfer property and the high oxidative capability of {1 1 1} crystal facets. The superior photoelectron transfer capability of the photoanodes was manifested by the inherent resistance (R_0) of the photoanodes using a simple photoelectrochemical method. The calculated R_0 values were 50.5 and 86.2 Ω for the rutile TiO_2 nanostructured film and anatase TiO_2 nanotube array film, respectively. Lower R_0 value of the rutile TiO_2 photoanode indicated a superior photoelectron transfer capability owing to good single crystal property of the rod-like rutile nanostructure. Almost identical valence band level (1.94 eV) of the rutile TiO_2 nanostructured film and anatase TiO_2 nanotube array film (meaning a similar oxidation capability) further confirmed the significant role of photoelectron transfer capability and exposed high-energy {1 1 1} crystal facets for improved photoelectrocatalytic performance of the rutile TiO_2 nanostructured film photoanode.

1. Introduction

Owing to excellent photocatalytic activity, titanium dioxide (TiO_2) has been widely investigated in varieties of applied fields such as environmental remediation, solar-driven hydrogen production, solar cells and lithium-ion batteries [1–10]. Although rutile TiO_2 possesses better chemical stability and UV absorption capability, anatase TiO_2 is more active for photocatalytic reaction than rutile TiO_2 ascribing to the more negative conduction band edge potential of anatase TiO_2, which is more favorable for reducing O_2 to $O_2^{\cdot-}$, greatly decreasing the recombination of photogenerated carriers [11–14]. The disadvantage of rutile TiO_2 with more positive conduction band edge potential has been the biggest limitation of rutile TiO_2 for photocatalytic application owing to high recombination of photogenerated carriers [14]. To solve this issue, our previous studies have demonstrated that a simple photoelectrochemical approach can be used to physically separate oxidation half-reaction (at the working electrode) and reduction half-reaction (at the auxiliary electrode) [15–17]. Using this approach, the applied potential bias can serve as an external driving force to timely remove the photogenerated electrons to the external circuit then to the counter electrode where the reduction-half reaction takes place [18,19]. Therefore, the recombination of photogenerated carriers can be effectively suppressed and the lifetime of photogenerated carriers (*e.g.*, photogenerated holes) is significantly improved, leading to high photocatalytic efficiency [15–17].

It is well known that the photocatalytic performance of TiO_2 photocatalyst is highly dependent on its size, morphology,

* Corresponding authors. Fax: +86 20 85290706 (T. An). Fax: +61 7 5552 8067 (H. Zhao).
E-mail addresses: antc99@gig.ac.cn (T. An), h.zhao@griffith.edu.au (H. Zhao).

http://dx.doi.org/10.1016/j.jcis.2014.05.012
0021-9797/

structure and crystal facet [20]. Specifically, TiO_2 crystal structures with uniquely exposed crystal facets have exhibited great potential in environmental remediation, water splitting of hydrogen production and solar energy conversion [21–23]. Recently, powder form rod-like rutile TiO_2 structures with exposed {1 1 1} top-facets and {1 1 0} side-facets have been developed, exhibiting excellent hydrogen production capability under visible light illumination [24]. Studies have indicated that the exposed {1 1 1} top-facets and {1 1 0} side-facets of rutile TiO_2 crystals can serve as oxidative and reductive sites for trapping photogenerated holes and electrons, respectively, which is favorable for inhibiting the recombination of the photogenerated carriers, improving the photocatalytic efficiency [25,26]. To employ photoelectrochemical technique for further improving photocatalytic efficiency, rutile TiO_2 nanostructured film with 100% exposed pyramid-shaped (1 1 1) surface has been fabricated onto FTO conductive glass substrate *via* a facile hydrothermal method by us [15–17]. The resulting rutile TiO_2 film as photoanode has shown superior photoelectrocatalytic performance toward oxidation of water and organics and bactericidal application under UV and visible light illumination ascribing to the superior photoelectron transfer property and high oxidative capability of the exposed {1 1 1} crystal facets of the rutile TiO_2 film [15–17]. To date, rutile TiO_2 nanostructures with exposed {1 1 1} crystal facets regardless of powder form or film form are exclusively synthesized by liquid-phase hydrothermal method [17,24]. Recently, our group developed a novel vapor-phase hydrothermal method to fabricate inorganic nanostructured materials [27–30]. The fabricated nanomaterials with unique structure displayed great application potential, which was unavailable using liquid-phase hydrothermal method owing to the distinct growth environment and mechanism of vapor-phase hydrothermal method [27–30]. Our studies indicated the feasibility of using vapor-phase hydrothermal method as a new synthetic method means to fabricate inorganic nanostructured materials with unique structure and property. Moreover, these nanostructured materials may be directly applied for energy generation and environment remediation.

Herein, rutile TiO_2 nanostructured film with exposed pyramid-shaped (1 1 1) surface was directly grown onto a titanium foil substrate *via* a facile vapor-phase hydrothermal method. Some experimental parameters such as the concentration of reaction precursors, reaction temperature and reaction time were investigated in detail to obtain the optimum experimental conditions. After calcination at 450 °C for 2 h in air, the fabricated rod-like rutile TiO_2 nanostructured film was directly used as photoanode for photoelectrocatalytic oxidation of water and decolorization of rhodamine B (RhB) under UV illumination. It should be noted that there is no published paper to date reported the photoelectrocatalytic decolorization of RhB on rutile TiO_2 nanostructured film with exposed pyramid-shaped (1 1 1) surface. For comparison, highly ordered anatase TiO_2 nanotube array film onto metal titanium foil substrate was also evaluated under the same experimental conditions.

2. Materials and methods

2.1. Synthesis

The rutile TiO_2 film with exposed pyramid-shaped (1 1 1) surface on titanium foil was synthesized by a simple vapor-phase hydrothermal method reported by us [27–30]. In a typical synthesis process, titanium foil (30 mm × 15 mm × 0.25 mm) was put on a Teflon holder which was about 3 cm above 10 mL of reaction solution containing 0.88 M H_2O_2 (30%, Sigma–Aldrich) and 4.6 M HCl (32%, Sigma–Aldrich). The subsequent reaction was carried out at 200 °C for 24 h. After the reaction, the autoclave was naturally cooled down to room temperature. Then, the titanium foil substrate was taken out, rinsed adequately with deionized water and dried at 60 °C for 12 h. The obtained sample was subsequently calcined in a tube furnace at 450 °C for 2 h in air with a heating rate of 2 °C min^{-1}. For comparison, highly ordered anatase TiO_2 nanotube array film was fabricated by anodization technique using metal titanium foil as substrate [31]. After anodization, the obtained nanotube film was thermally treated at 450 °C for 2 h in air for further photoelectrocatalytic application.

2.2. Characterization

The structural characteristics of the samples were investigated using X-ray diffractometer (XRD, Shimadzu XRD-6000, equipped with a graphite monochromatic Cu Kα), scanning electron

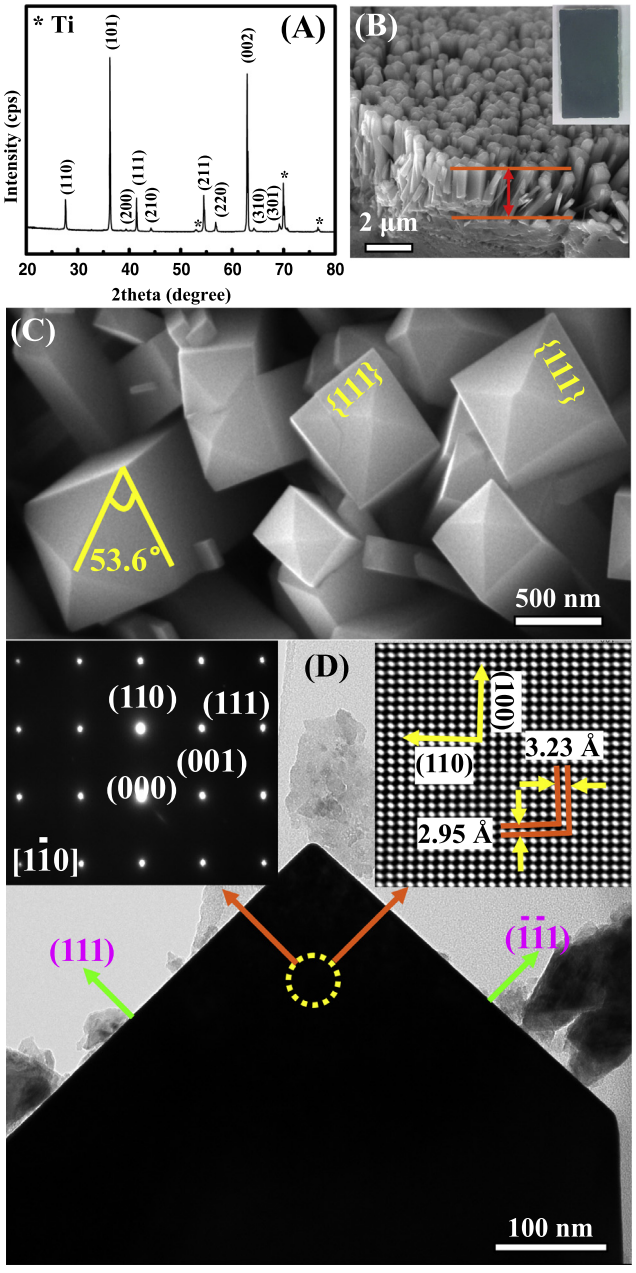

Fig. 1. XRD pattern (A), SEM ((B) cross-sectional, photograph and (C) surface of rutile film on titanium foil substrate) and TEM images of the prepared rutile TiO_2 film with exposed pyramid-shaped (1 1 1) surface.

microscope (SEM, JSM-6300F) and transmission electron microscope (TEM, Philips F20). The valence-band XPS spectra of the samples were analyzed by X-ray photoelectron spectroscopy (XPS, Kratos Axis ULTRA incorporating a 165 mm hemispherical electron energy analyzer). UV–vis diffuse reflectance spectra of the films were recorded on a Varian Cary 300 UV–vis–NIR spectrophotometer.

2.3. Measurements

The photoelectrochemical measurement was performed using a three-electrode system cell with a quartz window for illumination [16,17]. The prepared TiO_2 film was employed as a working electrode with a light illumination area of 0.785 cm^2, a platinum foil and a saturated Ag/AgCl as counter electrode and reference electrode, respectively. A 0.1 M $NaNO_3$ solution was used as supporting electrolyte. A voltammograph (CV-27, BAS) was used for the application of potential bias, while potential and current signals were recorded using a Macintosh (AD Instruments). UV illumination was carried out using a 150 W xenon arc lamp light source with focusing lenses (HF-200W-95, Beijing Optical Instruments). To avoid the electrolyte from being heated-up by the infrared light, a UV-band-pass filter (UG 5, Avotronics Pty. Ltd.) was used. The UV light intensity was regulated and carefully measured at 365 nm.

The directly photolytic, photocatalytic, electrocatalytic and photoelectrocatalytic decolorization of RhB were carried out in a similar three-electrode photoelectrochemical reactor with 60 mL of solution containing 0.1 M $NaNO_3$ and 2.0 mg L^{-1} RhB. The illuminated area of the photoanode was 1.766 cm^2. For PEC experiments, the applied potential was +0.8 V and the light intensity of UV was 3.0 mW cm^{-2}. The concentration of RhB after reaction was determined using the UV–vis spectrophotometer (UV-1800, Shimadu) at 554 nm.

The photoelectrocatalytic decolorization efficiency was calculated according to Eq. (1).

$$\text{Decolorization efficiency}\ (\%) = C/C_0 \times 100\% \quad (1)$$

where C presented the concentration of residual RhB after reaction and C_0 was original concentration of RhB.

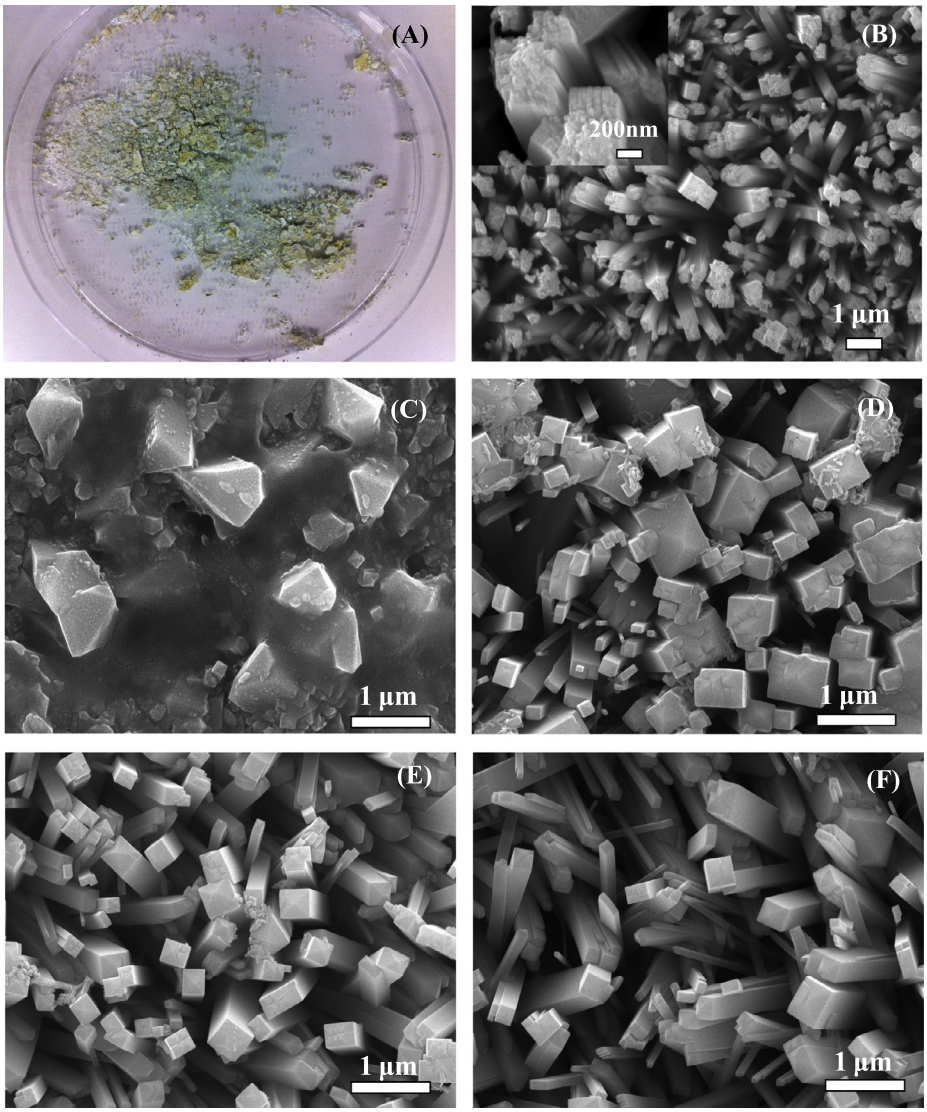

Fig. 2. Photograph of the sample obtained without H_2O_2 (A). SEM images of samples obtained at 180 °C for 24 h (B), with 1.5 M (C), 3.0 M (D), 6.1 M (E) and 7.6 M (F) HCl.

3. Results and discussion

3.1. Structure characteristics

Fig. 1A shows the XRD pattern of the prepared sample after calcination. Clearly, the diffraction peaks from the film can be indexed to a rutile phase TiO_2 with lattice parameters of $a = 4.584$ Å and $c = 2.953$ Å (JCPDS, card no. 89-4920) [16,24]. The morphology of the prepared rutile TiO_2 film is investigated by SEM technique, as shown in Fig. 1B and C. The cross-sectional SEM image indicates that the rutile TiO_2 film is consisted of vertically aligned rod-like arrays with diameters ranging from 400 to 700 nm and thickness of *ca.* 2.0 μm (Fig. 1B) and the film is well grown on the titanium foil substrate (inset in Fig. 1B). The surface SEM image shows rutile TiO_2 rod-like structures with surface exposed pyramid-shaped crystal facets (Fig. 1C). Further observation reveals that the angle between the bottom and lateral edges of the pyramid crystal facet is *ca.* 53.6°, matching closely to the theoretical value between the [1 1 0] and [0 1 1] directions for a tetragonal rutile TiO_2 [17,24]. TEM image as shown in Fig. 1D displays detailed structure information of an individual rutile TiO_2 rod-like structure. The selected area electron diffraction (SAED) and high-resolution TEM (HRTEM) image (insets in Fig. 1D) demonstrate a good single-crystal nature of the rutile TiO_2 structure. The SAED pattern reveals a preferred growth along the [0 0 1] direction of the rutile TiO_2 rod-like structure. The HRTEM image confirms the fringe spacings of 3.23 Å and 2.95 Å, which are consistent with the *d* values of (1 1 0) and (0 0 1) planes of the tetragonal rutile TiO_2, respectively [15–17]. Based on the above results, it can be confirmed that the top exposed pyramid-shaped crystal facets are {1 1 1} facets of rutile TiO_2, similar with the reported results [15–17].

To understand the formation process of the rutile TiO_2 film with exposed pyramid-shaped (1 1 1) surface on the titanium foil, the effect of reaction conditions on the resultant rutile TiO_2 morphology is investigated, as shown in Fig. 2. It is found that H_2O_2 plays an important role in the formation of high quality rutile TiO_2 film with exposed (1 1 1) surface on the titanium foil substrate (inset in Fig. 1B). In the absence of H_2O_2, the titanium foil is severely corroded and only fragments can be obtained after vapor-phase hydrothermal reaction (Fig. 2A). Similar results have also been addressed in our pervious work, indicating that the formation of peroxotitanium complex by Ti^{4+} reacting with H_2O_2 during the hydrothermal reaction can slow effectively the hydrolysis of the titanium precursor, which is favorable for the formation of {1 1 1} faceted rutile TiO_2 [16,17]. Further experiments demonstrate that rutile TiO_2 film with exposed high-quality (1 1 1) surface cannot

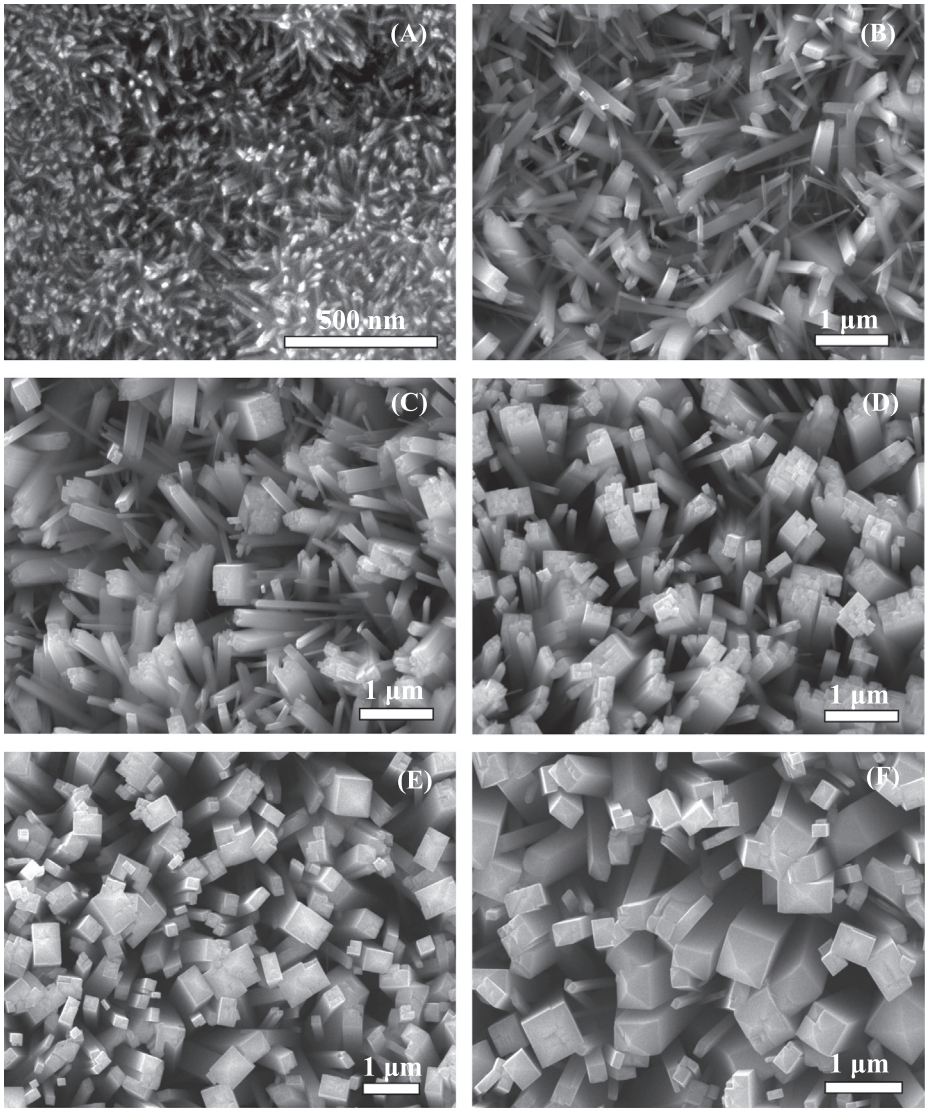

Fig. 3. SEM images of the samples obtained at different reaction times (A) 1 h; (B) 3 h; (C) 6 h; (D) 12 h; (E) 18 h; (F) 30 h.

be achieved when the reaction temperature is below 200 °C (*e.g.*, 180 °C, Fig. 2B).

In this work, the effect of hydrochloride acid (HCl) concentration on the resultant rutile TiO_2 morphology is also investigated in 10 mL of reaction solution containing 0.88 M H_2O_2 at 200 °C for 24 h. The corresponding SEM images are shown in Fig. 2C–F. When the HCl concentration is set at 1.5 M, a mixture of micro-sized and nano-sized protrudes can be observed on the titanium foil substrate (Fig. 2C). Increasing HCl concentration to 3.0 M (Fig. 2D), the independent rod-like structures can be obtained with incomplete {1 1 1} crystal facets and wide range of diameters. Further increasing HCl concentration to 4.6 M, high-quality rutile TiO_2 film with exposed pyramid-shaped (1 1 1) surface can be achieved (Fig. 1C). However, higher HCl concentration (*e.g.*, 6.1 and 7.6 M) is unfavorable for the formation of high-quality rutile TiO_2 film with exposed pyramid-shaped (1 1 1) surface, and only nanorod-like arrays with irregular surface can be observed, as shown in Fig. 2E and F. The above results demonstrate that an apt HCl concentration is critically important to fabricate high-quality rutile TiO_2 nanorod-like array film with exposed pyramid-shaped (1 1 1) surface using vapor-phase hydrothermal method. The optimal HCl concentration is chosen to be 4.6 M in this work.

With a reaction solution containing 4.6 M HCl and 0.88 M H_2O_2 and reaction temperature of 200 °C, the effect of hydrothermal reaction time on the morphology of the resultant rutile TiO_2 film is also studied. Fig. 3 shows the surface SEM images of the obtained products collected at different reaction intervals (1, 3, 6, 12, 18 and 30 h). Under high hydrothermal temperature (*e.g.*, 200 °C), metal titanium foil can readily react with HCl vapor to produce unstable Ti^{3+}, and then Ti^{3+} is instantly hydrated and oxidized by H_2O vapor to form Ti^{4+} on the substrate [32]. Subsequently, the formed Ti^{4+} reacts with H_2O_2 vapor to generate peroxotitanium complex which further hydrolyzes to form TiO_2 growth seeds. It can be seen from Fig. 3 that the density, diameter size and length of the obtained rod-like array structure obviously enhance with increasing hydrothermal time. Moreover, incomplete pyramid-shaped {1 1 1} crystal facets start to appear with prolonging hydrothermal reaction time (*e.g.*, 18 h, Fig. 3E). High-quality rutile TiO_2 film with exposed (1 1 1) surface can be achieved at hydrothermal reaction time of 24 h (Fig. 1C). Further increasing vapor-phase hydrothermal reaction time is not favorable for maintaining high-quality {1 1 1} crystal facets of rutile TiO_2 rod-like structures (*e.g.*, 30 h, Fig. 3F). The above investigations suggest that under the optimum conditions such as 10 mL of reaction solution containing 0.88 M H_2O_2 and 4.6 M HCl, reaction temperature of 200 °C and reaction time of 24 h, a high-quality rutile TiO_2 film with exposed pyramid-shaped (1 1 1) surface on the titanium foil can be obtained by a simple vapor-phase hydrothermal method.

3.2. Photoelectrocatalytic property

In previous report, our theoretical calculations have indicated that (1 1 1) surface of rutile TiO_2 is a high-energy surface, meaning high oxidative capability of the rutile TiO_2 film with exposed (1 1 1) surface [16]. In this work, the rutile TiO_2 film with exposed pyramid-shaped (1 1 1) surface onto metal titanium foil substrate was directly used as photoanode to evaluate its performance by photoelectrocatalytic oxidation of water and decolorization of RhB under UV irradiation. For comparison, highly ordered anatase TiO_2 nanotube array photoanode was also measured by photoelectrocatalytic oxidation of water and decolorization of RhB. Fig. 4 shows the XRD pattern and SEM image of the fabricated highly ordered TiO_2 nanotube array film after calcination at 450 °C for 2 h. As shown in Fig. 4A, anatase is predominant crystal phase of the TiO_2 nanotube arrays. The surface SEM image indicates that the fabricated anatase TiO_2 nanotubes possess outer diameters ranging from 70 to 100 nm, mean tube wall thickness of *ca.* 17 nm and film thickness of *ca.* 820 nm (Fig. 4B and inset). The SAED displays multiple diffraction rings of an individual nanotube, meaning that the wall of nanotube was composed by polycrystalline TiO_2 [33]. Although some studies have demonstrated that highly ordered nanotube structures can provide superior electron transfer pathways, the polycrystalline nanotube wall may be not beneficial for electron collection during electron transfer owing to the boundary scattering effect of polycrystalline nanoparticles [33].

Fig. 5A and B shows the voltammograms of the photoanodes made of rutile TiO_2 film and anatase TiO_2 nanotube film in 0.1 M $NaNO_3$ supporting electrolyte with or without UV illumination. As shown, without UV illumination, only a negligible dark current is measured for both rutile and anatase TiO_2 photoanodes. For the cases under UV illumination with different light intensities, the measured photocurrents (I_{ph}) increase linearly with applied potential bias in the range of low applied potential, and then reach saturated state (saturated photocurrent, I_{sph}) at higher applied potentials. This linearly increased I_{ph} in the range of low applied potential can be due to the limitation of free photoelectron transport within the TiO_2 photocatalyst films [33,34]. The saturated photocurrents at higher potentials (*ca.* 0.64 and 0.32 V for rutile TiO_2 film and anatase TiO_2 nanotube film, respectively) can be ascribed to the limitation of the interfacial processes at the photocatalyst/electrolyte interface [33,34]. Moreover, an increase in the saturated photocurrent is also observed as the light intensity

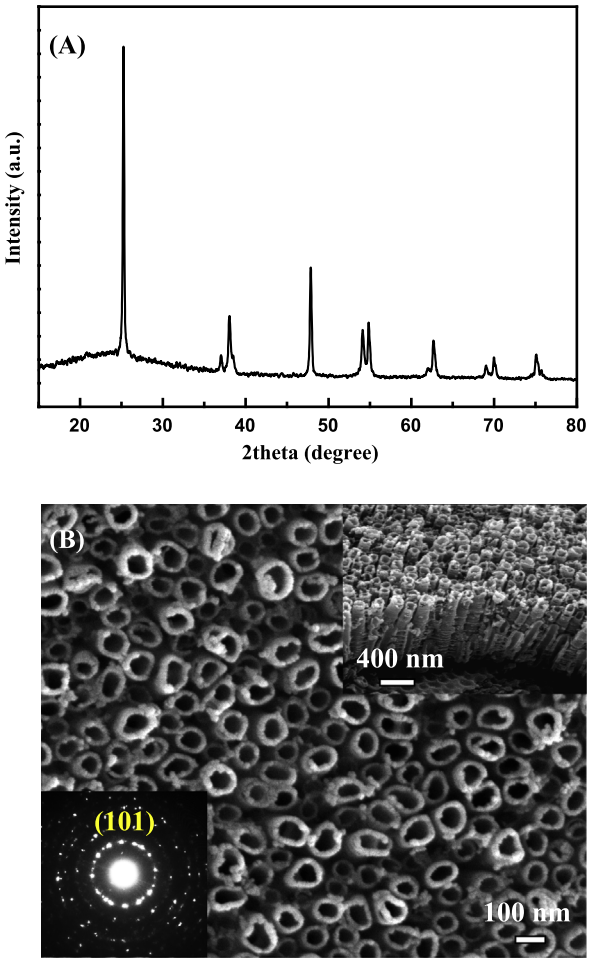

Fig. 4. (A) XRD pattern of the fabricated anatase TiO_2 nanotube arrays after calcination. (B) Surface SEM image of the fabricated anatase TiO_2 nanotube arrays after calcination; the top right inset of cross-sectional SEM image; the bottom left inset of SAED pattern of individual anatase nanotube.

increases, due to the stronger light intensity leading to the generation of more charge carriers [32]. Our previous studies have demonstrated that the magnitude of I_{sph} represents the maximum rate of water oxidation under a given light intensity [33,34]. Fig. 5C shows the plots of I_{sph} against the light intensity (φ) derived from Fig. 5A and B for rutile TiO_2 film and anatase TiO_2 nanotube film at +1.0 V of applied potential bias. Linear relationships with the slope values of 0.518 mA mW^{-1} (R^2 = 0.992) and 0.147 mA mW^{-1} (R^2 = 0.993) are obtained for rutile TiO_2 film and anatase TiO_2 nanotube film photoanodes, respectively. It is well known that the slope value of the I_{sph}–φ curve quantitatively represents the photoelectrocatalytic activity of the photoanode under the given experimental conditions. Clearly, the slope obtained from the photoanode made of rutile TiO_2 film is more than 3.5 times of that obtained from the anatase TiO_2 nanotube film photoanode, confirming significantly improved photoelectrocatalytic activity toward water oxidation of rutile TiO_2 film photoanode.

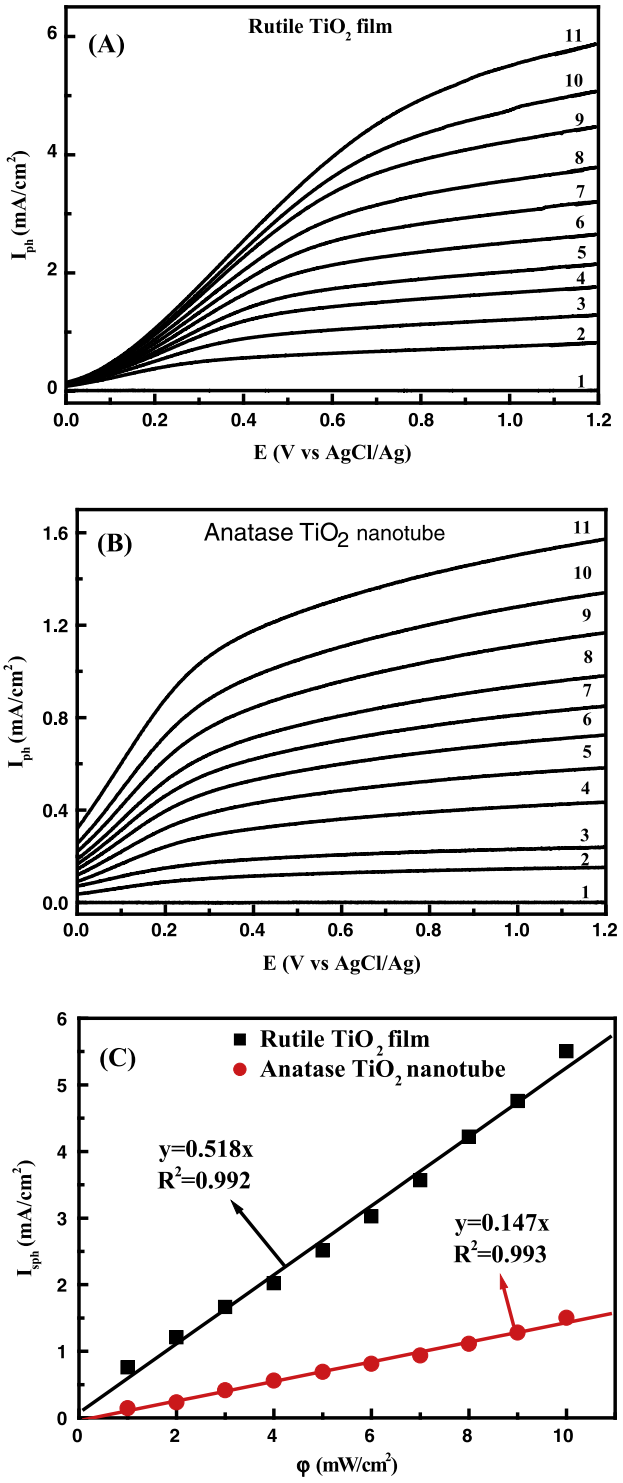

Fig. 5. Voltammograms obtained under different light intensities from rutile TiO_2 film (A) and anatase TiO_2 nanotube (B) photoanodes in 0.1 M $NaNO_3$ supporting electrolyte solution, respectively. The light intensity of curves 1–11, in turn, were 0, 1.0, 2.0, 3.0, 4.0, 5.0, 6.0, 7.0, 8.0, 9.0 and 10.0 mW cm^{-2}. (C) Relationships of saturation photocurrent with light intensity for rutile TiO_2 film and anatase TiO_2 nanotube photoanodes, respectively. The saturation photocurrent data were derived from the curves shown in A and B at +1.0 V of applied potential.

Fig. 6A displays directly photolytic (DP), electrocatalytic (EC), photocatalytic (PC) and photoelectrocatalytic (PEC) decolorization performances of RhB with or without TiO_2 photoanode and/or UV irradiation. Obviously, no obvious decolorization of RhB can be observed by EC process (applied potential of +0.8 V) within 150 min, while the decolorization efficiencies of RhB by DP and PC processes within 150 min are only 3.5% and 21.9%, respectively. A remarkable increase in the decolorization efficiency (92.0%) can be observed by PEC process within 150 min, which is more than 1.2 times of that (76.0%) using anatase TiO_2 nanotube photoanode by PEC technique. Furthermore, under the given experimental conditions, the photoelectrocatalytic decolorization of RhB using rutile TiO_2 and anatase TiO_2 nanotube photoanodes is of first order reaction. The calculated decolorization kinetic rate constants (k)

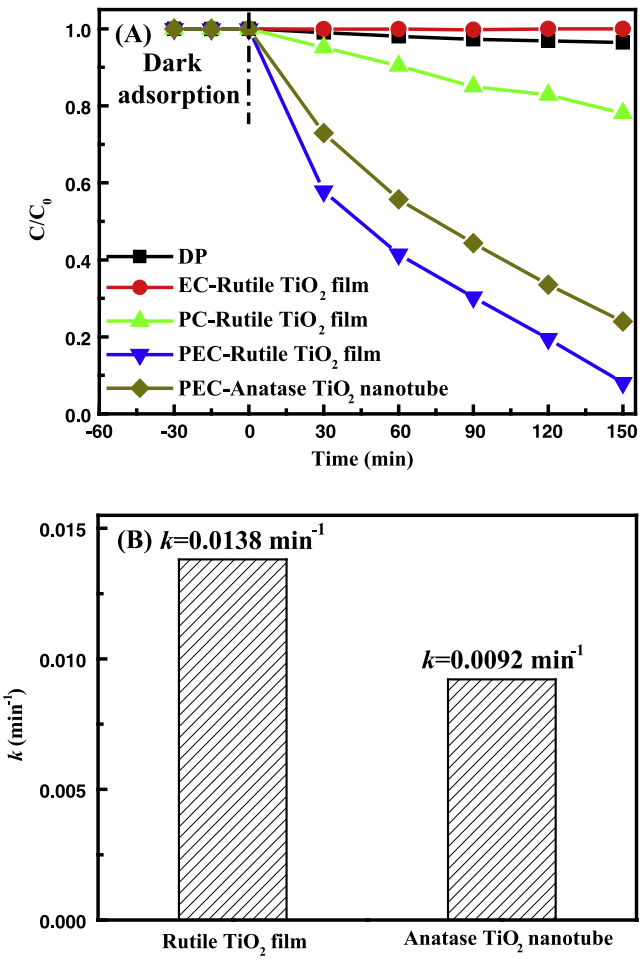

Fig. 6. (A) Decolorization kinetic curves of RhB under EC, DP, PC and PEC by the rutile TiO_2 film and anatase TiO_2 nanotube photoanodes. (B) The decolorization rate constants of the rutile TiO_2 film and anatase TiO_2 nanotube photoanodes for RhB. The applied potential was +0.8 V and the light intensity of UV was 3.0 mW cm^{-2}.

are 0.0138 and 0.0092 min^{-1} for rutile TiO_2 film and anatase TiO_2 nanotube photoanodes, respectively (Fig. 6B), indicating higher photoelectrocatalytic decolorization efficiency of rutile TiO_2 film photoanode than that of anatase TiO_2 nanotube film photoanode. This significantly improved photoelectrocatalytic efficiency of rutile TiO_2 film photoanode can be ascribed to many attributes, such as excellent photoelectron transport property and high oxidative capability of exposed pyramid-shaped (1 1 1) surface.

In our previous studies, the theoretical calculations have indicated that the pyramid-shaped (1 1 1) surface is a high-energy surface with a surface energy of 1.46 J/m^2, which is much higher than that (0.35 J/m^2) of routine rutile TiO_2 (1 1 0) surface [16], meaning high oxidative capability of the pyramid-shaped (1 1 1) surface. The high oxidative capability of the pyramid-shaped (1 1 1) surface is very favorable for improving the photoelectrocatalytic performance of the rutile TiO_2 film photoanode. Our previous studies have confirmed that the charge transport process inside of a photocatalyst layer can be manifested by the photocatalytic resistance of a photocatalyst – an intrinsic property of a semiconductor photocatalyst, which can be characterized quantitatively using a simple photoelectrochemical method [34,35]. In this work, the intrinsic resistance (R_0) of photoanodes made of rutile TiO_2 film and anatase TiO_2 nanotube film is measured to reveal the photoelectron transport property of these two TiO_2 photocatalyst films. As discussed above, the voltammograms shown in Fig. 5A and B include two parts, namely, linear increase part and leveled off part. The former exhibits a pure resistor-type behavior, suggesting that the whole reaction is controlled by the photoelectron transport process inside the photocatalyst layer [34,35]. Thus, the photocurrent is determined by the rapidity of the photoelectron transport across the photocatalyst layer [34,35]. The overall resistance (R) values of the voltammograms under different light intensities can be calculated in accordance with the Ohm law by dividing the potential change by the corresponding photocurrent within the linear part of the voltammograms [34,35]. Plotting R against I_{sph} derived from Fig. 5A and B gives the hyperbolic curve as shown in Fig. 7A and B for rutile TiO_2 film and anatase TiO_2 nanotube film photoanodes, respectively. The quantitative relationship between R and I_{sph} can be expressed as [16]:

$$R = k/I_{sph} + R_0 = R_I + R_0 \quad (2)$$

where k is a proportionality constant; I_{sph} is the saturation photocurrent at a constant potential bias (+1.0 V in this work); R_0 and R_I are the constant and the variant components of the resistance, respectively.

From Eq. (2), R is the total reaction resistance, which is the sum of a variant ($R_I = k/I_{sph}$) and a constant (R_0) component. For a given photoanode, R_I represents the interfacial reaction resistance, depending on experimental conditions, such as light intensity and reactant concentration, while R_0 collectively represents an intrinsic

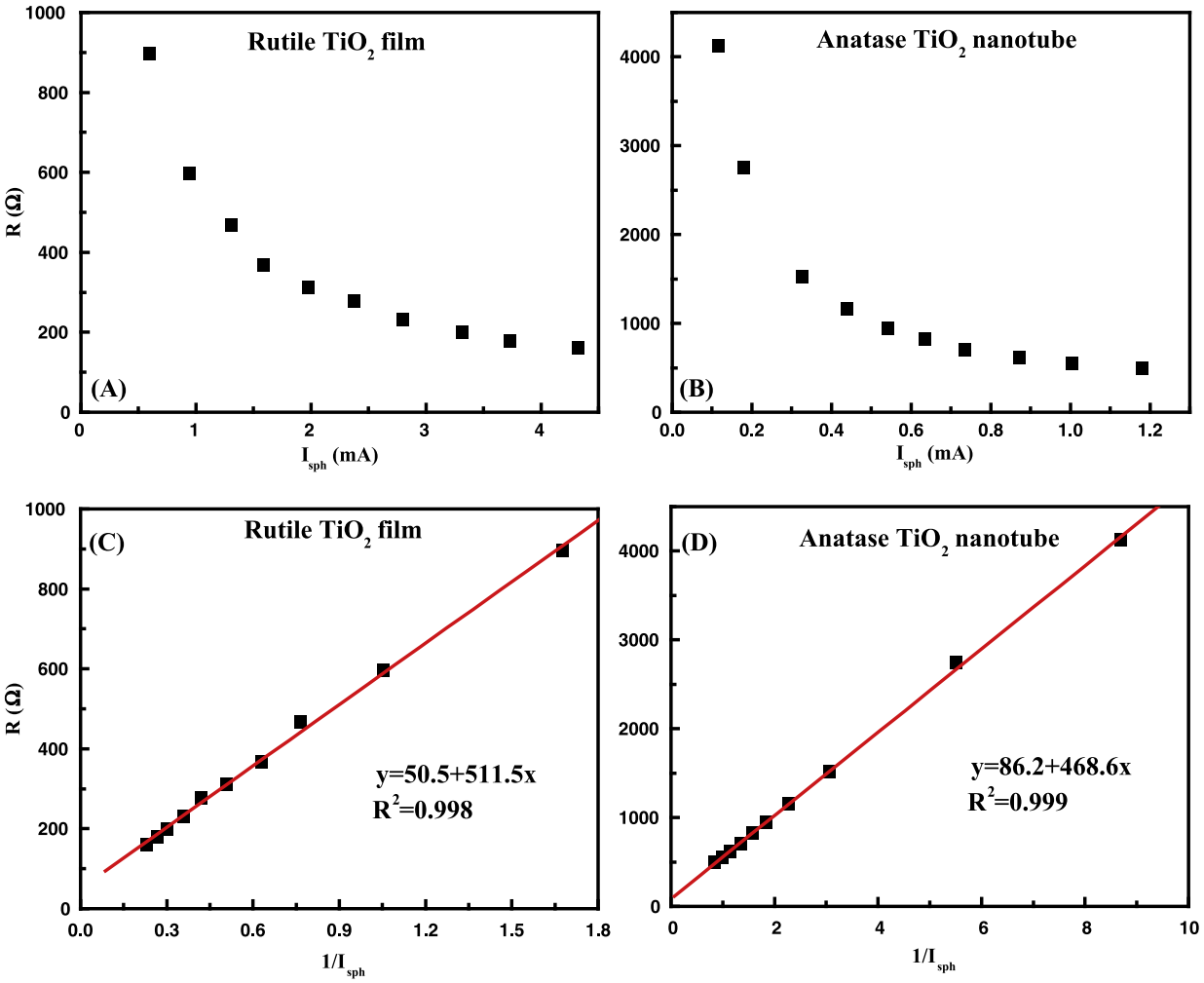

Fig. 7. Relationships between the resistance and the saturation photocurrent measured with the rutile TiO_2 film (A) and anatase TiO_2 nanotube (B) photoanodes. Relationships between the resistance and the inversed saturation photocurrent with the rutile TiO_2 film (C) and anatase TiO_2 nanotube (D) photoanodes. Data were derived from Fig. 5A and B.

property of a TiO_2 photocatalyst reflecting photoelectron transport process inside TiO_2 photocatalyst layer [16]. This intrinsic R_0 value is independent of experimental conditions [16,33]. Fig. 7C and D display the plots of R against $1/I_{sph}$ values for rutile TiO_2 film and anatase TiO_2 nanotube film photoanodes. As shown, plotting R against $1/I_{sph}$ gives a straight line for both photoanodes, indicating that the variant resistance component is inversely proportional to I_{sph}. R_0 values for the two photoanodes can be obtained from the intercepts of the curves with a value of 50.5 and 86.2 Ω for rutile TiO_2 film and anatase TiO_2 nanotube film photoanodes, respectively. The obtained k values are 511.5 and 468.6 Ω mA for rutile TiO_2 film and anatase TiO_2 nanotube film photoanodes, respectively. The physical meaning of the slope, k, can be explained as the minimum applied potential bias required to remove 100% of the photogenerated electrons from the photocatalyst layer [34]. The higher k value (511.5 Ω mA) for the rutile TiO_2 film photoanode over the anatase TiO_2 film photoanode (468.6 Ω mA) can be attributed to the more positive conduction band edge potential of the rutile TiO_2 [33]. Meanwhile, the rutile TiO_2 film photoanode has almost 42% lower than R_0 (50.5 Ω) in comparison with that of the anatase TiO_2 nanotube photoanode with an intrinsic R_0 = 86.2 Ω, owing to the superior single crystal property of the rutile TiO_2 rod-like structure. The anatase TiO_2 nanotube is composed of polycrystals, which enhances the photoelectron scattering effect resulting in higher R_0 value at the crystalline boundaries [33]. The superior photoelectron transfer property contributes significantly improved photoelectrocatalytic activity toward water oxidation and RhB decolorization of the rutile TiO_2 film photoanode.

It is well known that the photoelectrocatalytic oxidation capacity of a photocatalyst is mainly determined by its valence band edge potential [33]. In this work, the electronic band structures of the rutile TiO_2 film and the anatase TiO_2 nanotube film photoanodes are therefore investigated. Fig. 8A shows the UV–vis diffuse reflection spectra of these two photoanodes. As shown, an obvious redshift in the band gap absorption edge for the rutile TiO_2 film versus the anatase TiO_2 nanotube film is observed and the calculated band gaps of the rutile TiO_2 film and anatase TiO_2 nanotube film are around 2.94 eV and 3.22 eV, respectively. Fig. 8B shows XPS valence-band (VB) spectra of the rutile TiO_2 film and anatase TiO_2 nanotube film. The VB spectra reveal that the VB maximum of these two TiO_2 films is almost identical (*ca.* 1.94 eV) [33,36,37], indicating the same valence band edge position of these two TiO_2 films. Similar results have also been reported by Zhao et al. [33] and Hagfeldt et al. [38]. Based on the above results, the conduction band (CB) minimum of the anatase TiO_2 nanotube film is calculated to be 0.28 eV more negative than that of the rutile TiO_2 film. The electronic band structures of these two TiO_2 films are illustrated in Fig. 8C. The almost identical valence band edge position means a similar photocatalytic oxidation capacity for these two TiO_2 films because only an oxidative process can occur at the photoanode film, and the conduction band edge position has not been a limiting factor for the photocatalytic activity of photoanode using a photoelectrochemical approach [33]. The XPS VB data also indicate that the rutile TiO_2 film photoanode has sufficient photocatalytic oxidation capacity toward water and RhB that is similar to the anatase TiO_2 nanotube photoanode, while the low intrinsic resistance (R_0, representing superior photoelectron transport capability) of the rutile TiO_2 film contributes significantly to the high photoelectrocatalytic activity toward water oxidation and RhB decolorization in this study.

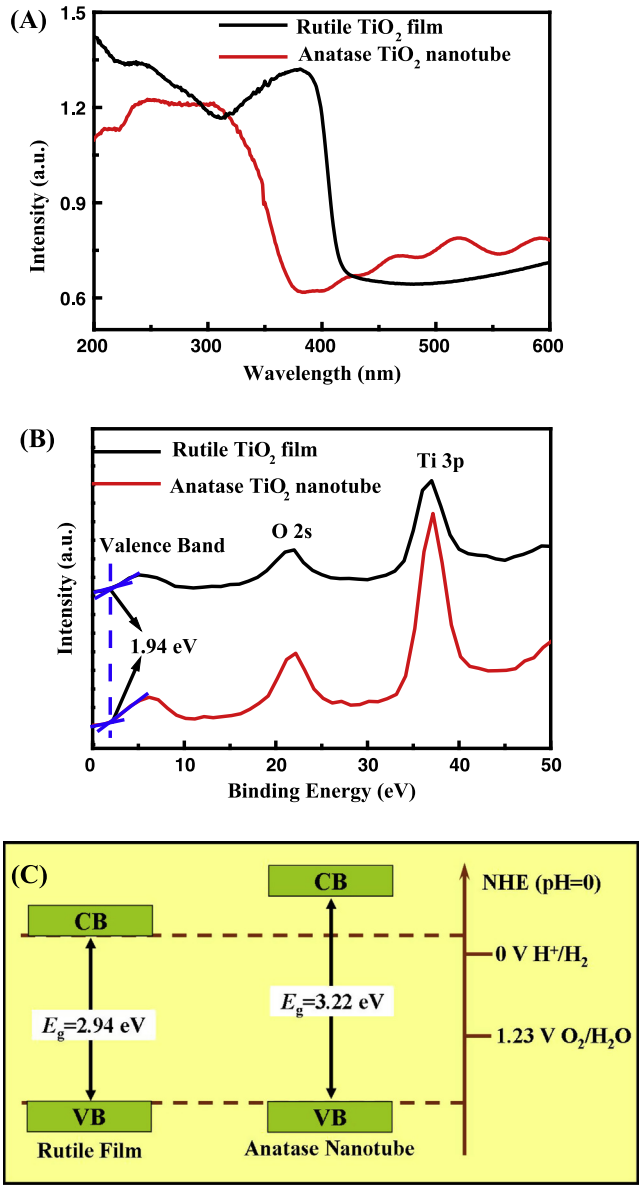

Fig. 8. (A) UV–vis absorption spectra of the rutile TiO_2 film and anatase TiO_2 nanotube. (B) XPS valence-band spectra of the rutile TiO_2 film and anatase TiO_2 nanotube. (C) Determined valence-band and conduction-band edges of the rutile TiO_2 film and anatase TiO_2 nanotube photoanodes.

4. Conclusion

High-quality rutile TiO_2 film with exposed pyramid-shaped (1 1 1) surface has been directly grown on titanium foil by using a simple vapor-phase hydrothermal method. The obtained rutile TiO_2 film as photoanode exhibited superior photoelectrocatalytic activity toward water oxidation and RhB decolorization. XPS valence-band spectra indicated that the rutile TiO_2 film had almost identical valence band position with the anatase TiO_2 nanotube film, meaning a similar oxidation capability. However, the lower intrinsic resistance (R_0) of the rutile TiO_2 film contributed to more than 3.5 and 1.2 times higher photoelectrocatalytic activity toward water oxidation and RhB decolorization than the anatase TiO_2 nanotube film, indicating the superior photoelectron transport property of the rutile TiO_2 film.

Acknowledgments

This is Contribution No. IS-1887 from GIGCAS. This work was financially supported by the Australian Research Council (ARC) Discovery Project and NSFC (21307132, 41373102 and 21077104).

References

[1] M.R. Hoffmann, S.T. Martin, W.Y. Choi, D.W. Bahnemann, Chem. Rev. 95 (1995) 69–96.
[2] X.B. Chen, L. Liu, P.Y. Yu, S.S. Mao, Science 331 (2011) 746–750.
[3] S.A. Berhe, S. Nag, Z. Molinets, W.J. Youngblood, ACS Appl. Mater. Inter. 5 (2013) 1181–1185.
[4] C.Y. Cho, J.H. Moon, Langmuir 28 (2012) 9372–9377.
[5] J.D. Zhuang, W.X. Dai, Q.F. Tian, Z.H. Li, L.Y. Xie, J.X. Wang, P. Liu, X.C. Shi, D.H. Wang, Langmuir 26 (2010) 9686–9694.
[6] X.F. Yang, J.L. Qin, Y. Li, R.X. Zhang, H. Tang, J. Hazard. Mater. 261 (2013) 342–350.
[7] J.Y. Chen, G.Y. Li, Z.G. He, T.C. An, J. Hazard. Mater. 190 (2011) 416–423.
[8] D.W. Jing, L. Jing, H. Liu, S. Yao, L.J. Guo, Ind. Eng. Chem. Res. 52 (2013) 1982–1991.
[9] H.E. Wang, J. Jin, Y. Cai, J.M. Xu, D.S. Chen, X.F. Zheng, Z. Deng, Y. Li, I. Bello, B.L. Su, J. Colloid Interface Sci. 417 (2014) 144–151.
[10] V.K. Gupta, R. Jain, S. Agarwal, A. Nayak, M. Shrivastava, J. Colloid Interface Sci. 366 (2012) 135–140.
[11] J.Y. Chen, X. Nie, H.X. Shi, G.Y. Li, T.C. An, Chem. Eng. J. 228 (2013) 834–842.
[12] M. Hussain, R. Ceccarelli, D.L. Marchisio, D. Fino, N. Russo, F. Geobaldo, Chem. Eng. J. 157 (2010) 45–51.
[13] S.S. Watson, D. Beydoun, J.A. Scott, R. Amal, Chem. Eng. J. 95 (2003) 213–220.
[14] L. Sun, Y. Qin, Q.Q. Cao, B.Q. Hu, Z.W. Huang, L. Ye, X.F. Tang, Chem. Commun. 47 (2011) 12628–12630.
[15] X.L. Liu, H.M. Zhang, C. Liu, J.Y. Chen, G.Y. Li, T.C. An, H.J. Zhao, Catal. Today 224 (2014) 77–82.
[16] H.M. Zhang, X.L. Liu, Y. Wang, P.R. Liu, W.P. Cai, G.S. Zhu, H.G. Yang, H.J. Zhao, J. Mater. Chem. A 1 (2013) 2646–2652.
[17] X.L. Liu, H.M. Zhang, X.D. Yao, T.C. An, P.R. Liu, Y. Wang, F. Peng, A.R. Carroll, H.J. Zhao, Nano Res. 5 (2012) 762–769.
[18] K. Vinodgopal, S. Hotchandani, P.V. Kamat, J. Phys. Chem. – US 97 (1993) 9040–9044.
[19] M. Tian, G.S. Wu, B. Adams, J.L. Wen, A.C. Chen, J. Phys. Chem. C 112 (2008) 825–831.
[20] K.L. Lv, Q.J. Xiang, J.G. Yu, Appl. Catal. B – Environ. 104 (2011) 275–281.
[21] T.C. An, J.Y. Chen, X. Nie, G.Y. Li, H.M. Zhang, X.L. Liu, H.J. Zhao, ACS Appl. Mater. Inter. 4 (2012) 5988–5996.
[22] H.M. Zhang, Y. Wang, P.R. Liu, Y.H. Han, X.D. Yao, J. Zou, H.M. Cheng, H.J. Zhao, ACS Appl. Mater. Inter. 3 (2011) 2472–2478.
[23] H.M. Zhang, Y.H. Han, X.L. Liu, P.R. Liu, H. Yu, S.Q. Zhang, X.D. Yao, H.J. Zhao, Chem. Commun. 46 (2010) 8395–8397.
[24] F. Zuo, K. Bozhilov, R.J. Dillon, L. Wang, P. Smith, X. Zhao, C. Bardeen, P.Y. Feng, Angew. Chem. Int. Ed. 51 (2012) 6223–6226.
[25] P.M. Oliver, G.W. Watson, E.T. Kelsey, S.C. Parker, J. Mater. Chem. 7 (1997) 563–568.
[26] N. Murakami, A. Ono, M. Nakamura, T. Tsubota, T. Ohno, Appl. Catal. B – Environ. 97 (2010) 115–119.
[27] P.R. Liu, Y. Wang, H.M. Zhang, T.C. An, H.G. Yang, Z.Y. Tang, W.P. Cai, H.J. Zhao, Small 8 (2012) 3664–3673.
[28] H.M. Zhang, Y.B. Li, P.R. Liu, Y. Li, D.J. Yang, H.G. Yang, H.J. Zhao, Chem. – Eur. J. 18 (2012) 5165–5169.
[29] P.R. Liu, H.M. Zhang, H.W. Liu, Y. Wang, T.C. An, W.P. Cai, H.G. Yang, X.D. Yao, G.S. Zhu, R. Webb, H.J. Zhao, Small 9 (2013) 3043–3050.
[30] P.R. Liu, H.M. Zhang, H.W. Liu, Y. Wang, X.D. Yao, G.S. Zhu, S.Q. Zhang, H.J. Zhao, J. Am. Chem. Soc. 133 (2011) 19032–19035.
[31] J.M. Macak, P. Schmuki, Electrochim. Acta 52 (2006) 1258–1264.
[32] Q. Zhou, X.F. Yang, S.Q. Zhang, Y.X. Han, G.F. Ouyang, Z.H. He, C.L. Liang, M.M. Wu, H.J. Zhao, J. Mater. Chem. 21 (2011) 15806–15812.
[33] H.M. Zhang, X.L. Liu, Y.B. Li, Q.F. Sun, Y. Wang, B.J. Wood, P.R. Liu, D.J. Yang, H.J. Zhao, J. Mater. Chem. 22 (2012) 2465–2472.
[34] H.M. Zhang, H.J. Zhao, S.Q. Zhang, X. Quan, ChemPhysChem 9 (2008) 117–123.
[35] H. Yu, S.Q. Zhang, H.J. Zhao, H.M. Zhang, Phys. Chem. Chem. Phys. 12 (2010) 6625–6631.
[36] J. Pan, G. Liu, G.M. Lu, H.M. Cheng, Angew. Chem. Int. Ed. 50 (2011) 2133–2137.
[37] G.L. Zheng, J. Wang, X.L. Liu, A.L. Yang, H.P. Song, Y. Guo, H.Y. Wei, C.M. Jiao, S.Y. Yang, Q.S. Zhu, Z.G. Wang, Appl. Surf. Sci. 256 (2010) 7327–7330.
[38] A. Hagfeldt, G. Boschloo, L.C. Sun, L. Kloo, H. Pettersson, Chem. Rev. 110 (2010) 6595–6663.